
Modelling of gain profiles and Raman lasing in TiO₂/GeO₂-doped silica fibres

Felinskyi G. S., Grygoruk V. I. and Serdeha I. V.

Kyiv National Taras Shevchenko University, 64/13 Volodymyrska Street, 01601 Kyiv, Ukraine. ivserdega@gmail.com

Received: 14.01.2020

Abstract. We analyze Raman lasing bandwidth for TiO₂-doped single-mode fibre as a function of pumping power, following from modelling of the gain profile, and compare it with that typical for an etalon Raman (GeO₂-doped) fibre. The both Raman gain profiles are quantified using the spontaneous Raman cross-sections derived with an original spectroscopic method. Extremely high accuracy of the multimode Gaussian decomposition is obtained for the Raman gain profiles. As a result, the Raman gain profiles can be presented in analytical form. A threshold spectral Raman profile is introduced and the lasing bands in the both single-mode fibres are simulated numerically. We discuss also the advantages of TiO₂-doped fibres as the active media for fibre Raman lasing and compare their characteristics with those of the other fibre types.

Keywords: Raman lasing, gain profile, Gaussian decomposition, Raman gain threshold, nonlinear optical amplification

UDC: 535.375+ 621.373.8

1. Introduction

Progress in the field of optical fibres is usually achieved in close collaboration of waveguide and materials engineers [1]. While earlier efforts of developers have been mainly focused on the novel waveguide designs, nowadays we witness a clear emphasis on the studies of fibre materials, in particular, as active media for optical amplification [1, 2]. A continuous worldwide exponential growth in the demands for optical fibre transmission is now satisfied by applications of fibre Raman amplifiers. Indeed, the use of single ultra-long-span links as long as several hundred kilometres is extended steadily. It is firmly confirmed [3] that ultra-long-span unrepeated systems that employ distributed Raman amplifiers represent a simple and cost-effective solution that does not require active in-line components. The transmission performance can be enhanced by improvements in the design of fibre-optic core and material characteristics [4], including the fibres with large effective-core area [5] and very low-loss fibres [6]. Simultaneously with application of fibre Raman amplifiers, the propagation distance for unrepeated systems is being extended, with no discrete active devices. It is the ability to provide distributed amplification within the transmission fibre [7] that represents the main advantage of Raman amplifiers over the other optical amplifier types such as erbium-doped fibres or semiconductor optical amplifiers. Distributed Raman amplification scheme has been used [8] to reach 10×116 Gb/s DP-QPSK WDM data transmission on a distances up to 7915 km. Recently, the researchers have achieved reliable transfer of optical data after 6000 km transmission with 9 Tb/s capacity, using the Raman amplifiers [9].

Modern progress in the development of fibre lasers in terms of their working spectrum, emitting linewidth, output power and pulse energy is essentially determined by special dopants

incorporated in fibre core. The output power of fibre-optical sources based on both rare-earth-doped fibres [10–12] and Raman lasers [13, 14] has been increased dramatically over the past decade. In particular, a short piece (~ 30 m) of standard single-mode silica fibre has been used in Ref. [15] in a fibre Raman laser (FRL).

Traditionally the FRL systems are produced using germano-silicate fibres as an active medium for stimulated Raman light emission [16–18]. Their main advantage is higher Raman scattering cross-section, when compared to the other silica fibres [19]. A GeO_2 -doped fibre has been used both for the Raman amplification of optical signals and in the fibre lasers [20, 21]. A high-power FRL has been demonstrated recently in Ref. [22], with the 1.28 kW c. w. output power obtained using a piece of 70 m-long germanium-doped fibre. Furthermore, the GeO_2 -doped fibre is a key element in highly efficient Raman wavelength converters from 1080 to 1120 nm. Earlier we have presented [23] a detailed analysis of Raman lasing threshold and generation bandwidth for the GeO_2 -doped single-mode fibre (SMF). Since the Raman properties of this fibre are well studied, we use the GeO_2 -doped fibre as a Raman etalon in our studies of TiO_2 -doped fibre.

Notice that the Raman properties of the other fibre types and, in particular, of TiO_2 -doped silica SMFs have not yet been studied sufficiently. In the present work, we apply an original spectroscopic method to determine quantitatively the Raman properties of the GeO_2 - and TiO_2 -doped SMFs. A primary aim of our study is to compare the Raman gain profiles for these fibres in analytical form and obtain the lasing bandwidths for the $\text{TiO}_2/\text{GeO}_2$ -doped silica fibres.

2. Modelling background and experimental data processing

The ranges of Stokes shifts found in the Raman spectra of the optical fibres based on amorphous silica glass are extremely wide. They extend continuously and irregularly over more than 1000 cm^{-1} (i.e., 30 THz). The shift is formed by several unresolved phonon bands due to strongly overlapping and widened spectral lines up to $100\text{ cm}^{-1} \cong 3.3\text{ THz}$ (see Fig. 1a and Fig. 1b). Thus, high-quality amplification of optical signals can be made with the working frequency bandwidth of at least 10 THz, using a stimulated Raman effect. Accordingly, ultra-wideband FRAs with very low self-noises have already been implemented with pumping at several wavelengths.

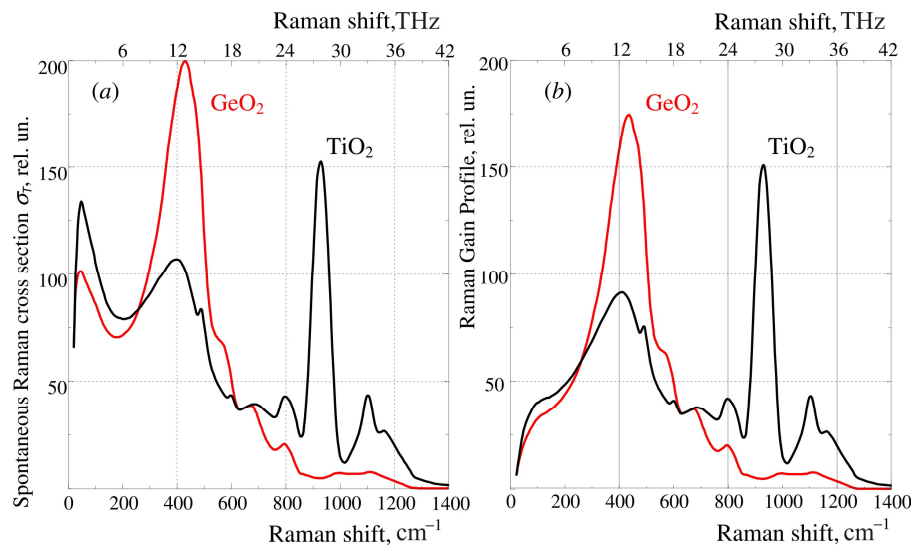


Fig. 1. Spontaneous Raman spectrum (a) and gain profile (b) for TiO_2 -doped fibre as compared with the corresponding data for germanium-silicate single-mode fibre.

On the other hand, a ‘diffuse’ nature of amplification spectra complicates significantly any attempts to model the Raman gain profiles. This needs implementation of some special spectroscopic techniques.

2.1. Theoretical basis for determination of Raman gain profile

It is well known [21] that the stimulated Raman scattering does not depend on temperature. Then the Raman gain profile $g_R(\omega)$ is also temperature-independent. On the other hand, $g_R(\omega)$ can be expressed using the spontaneous Raman cross-section $\sigma_0(\omega)$ determined at $T = 0$ as

$$g_R(\omega) = \sigma_0(\omega) \cdot \frac{\lambda_s^3}{c^2 h A_{eff}^{ps} n_p^2}, \quad (1)$$

where λ_s is the Stokes wavelength, c the speed of light in vacuum, h the Planck constant, A_{eff}^{ps} the effective area of the region where the pumping and signal waves are overlapped, and n_p the refractive index actual at the pumping wavelength.

The spontaneous cross-section $\sigma_T(\omega)$ at $T > 0$ refers to a zero-temperature Raman cross-section $\sigma_0(\omega)$ as

$$\sigma_0(\omega) = \frac{\sigma_T(\omega)}{n_B(\omega, T) + 1}, \quad (2)$$

where $n_B(\omega, T) = [\exp(\hbar\omega / k_B T) - 1]^{-1}$ is the Bose–Einstein factor and k_B the Boltzmann constant.

Fig. 1 shows the difference between the spontaneous Stokes spectra (Fig. 1a) and the Raman gain profiles (Fig. 1b) obtained at the room temperature for the GeO₂-doped and TiO₂-doped single-mode silica fibres. All the spectra in Fig. 1 are normalized to the spontaneous Raman spectrum for the GeO₂-doped fibre, where the maximal Stokes intensity $I_{max}(\text{GeO}_2)$ is observed at the main peak located at 430 cm⁻¹. The Raman gain profiles are obtained with taking Eqs. (1) and (2) into account. They are shown in Fig. 1b with the relative intensity of TiO₂ spectrum fixed with respect to the etalon Stokes spectrum of GeO₂.

Note that essentially multimode spontaneous Raman spectrum is observed for the TiO₂-doped fibre, whereas its absolute intensity maximum $I_{max}(\text{TiO}_2)$ is detected at the frequency 930 cm⁻¹. Comparing the both spontaneous Stokes spectra, we have found directly the ratio $I_{max}(\text{GeO}_2)/I_{max}(\text{TiO}_2) = 1.3042$. Then the Raman gain profiles for the TiO₂-doped fibre can be quantified based on the known Raman gain data for TiO₂ [19] as a reference.

2.2. Analytic form of Raman gain profile

We have performed a standard decomposition into vibrational modes for a complicated Raman spectrum in a manner different from the standard one. Namely, we have solved this problem in order to represent the spectrum in analytical form [23]. This application of the decomposition differs from its common purpose, interpretation of experimental Raman gain data and classification of associated oscillators. In accordance with spectroscopic classification, each phonon mode in the case of homogeneous broadening should be observed as a pure linear oscillator (of a Lorentz type). Alternatively, it can be described with a Gauss lineform in the case of nonuniform broadening. Since every vibration in the fused silica glass suffers extreme broadening, our modelling has proved that the Gaussian decomposition results in essentially higher accuracy, if compared with a common oscillator approximation.

Therefore all the Raman gain profiles in our work are decomposed with the Gaussian

components as

$$g_R(\omega) = \sum_{i=1}^N A_i \exp\left[-\frac{(\omega - \omega_{v,i})^2}{\Gamma_i^2}\right], \quad (3)$$

where N implies the number of Gaussian vibrational modes, $\omega_{v,i}$ the central frequency for the i -th mode, $\Gamma_i \approx 0.6 \cdot \text{FWHM}_i$ the dumping constant, FWHM_i the full width at half maximum for the i -th mode, and A_i the phonon amplitude.

To avoid well-known ambiguities in the interpretation of phonon spectra, we have performed decomposition procedures for an arbitrary number of Gaussian components. Our principal aim has been maximizing the fitting accuracy for all the experimental profiles. The main decomposition results for the Raman gain profiles are presented in Table 1 and Table 2 respectively for the reference GeO₂-doped silica fibre and the TiO₂-doped fibre. The fitting parameters A_i , $\omega_{v,i}$ and Γ_i represent a complete set of parameters needed for representation of the Raman gain profiles in analytical form using Eq. (3).

Table 1. Results of Gaussian decomposition of the Raman gain profile for GeO₂-doped silica fibre in the region 20–1200 cm⁻¹: A_i denote amplitudes, $\omega_{v,i}$ frequencies and Γ_i dumping constants.

Mode No	GeO ₂ $g_{Rmax}=6.3 (W \cdot km)^{-1} *$		
	A_i	$\omega_i [cm^{-1}]$	$\Gamma_i [cm^{-1}]$
G ₁	0.04	48	25
G ₂	0.09	89	53
G ₃	0.18	179	102
G ₄	0.49	360	119
G ₅	0.68	448	80
G ₆	0.08	481	21
G ₇	0.25	573	43
G ₈	0.21	670	71
G ₉	0.09	796	48
G ₁₀	0.04	996	175
G ₁₁	0.02	1133	81

* Data of the Raman gain peak value taken from Ref. [19]

Table 2. Results of Gaussian decomposition of the Raman gain profile for TiO₂-doped silica fibre in the region 20–1200 cm⁻¹: A_i denote amplitudes, $\omega_{v,i}$ frequencies and Γ_i dumping constants.

Mode No	TiO ₂ $g_{Rmax}=4.8 (W \cdot km)^{-1} *$		
	A_i	$\omega_i [cm^{-1}]$	$\Gamma_i [cm^{-1}]$
G ₁	0.11	67	38
G ₂	0.13	130	75
G ₃	0.53	381	215
G ₄	0.09	418	56
G ₅	0.07	493	14
G ₆	0.03	599	16
G ₇	0.19	712	94
G ₈	0.21	811	41
G ₉	1.00	928	44
G ₁₀	0.13	1097	26
G ₁₁	0.17	1135	115
G ₁₂	0.02	1173	20

* Our estimation is referred to GeO₂ SMF (see Fig. 1b)

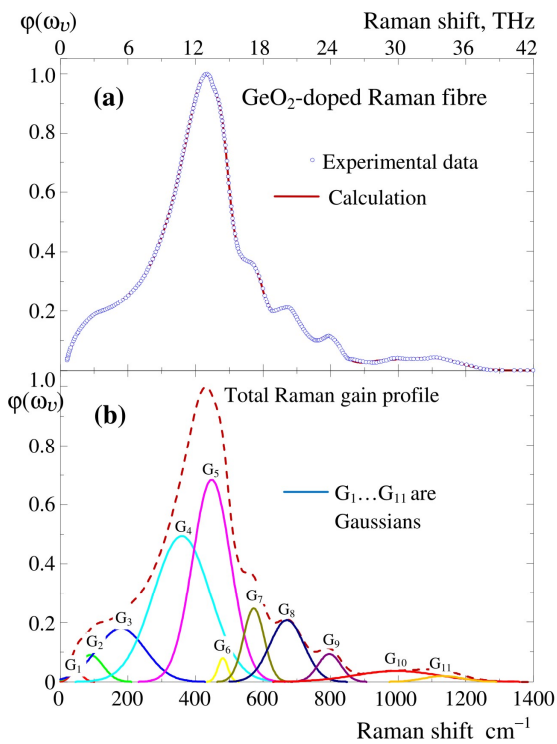


Fig. 2. Multimode Gaussian decomposition for GeO_2 -doped silica fibre. Panel (a) shows experimental Raman gain profile (blue circles) and its fit (red solid line) obtained with Eq. (3), and panel (b) displays overall fitted spectrum (dotted line) and eleven Gaussian components (solid lines of different colours).

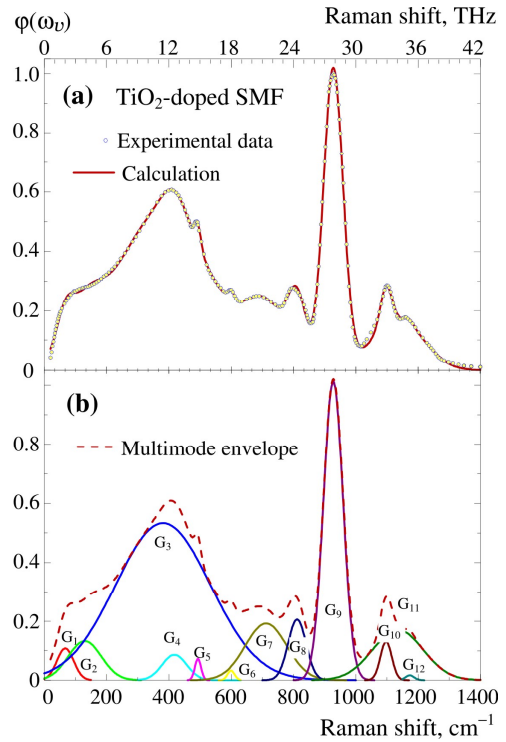


Fig. 3. Multimode Gaussian decomposition for TiO_2 -doped silica fibre. Panel (a) shows experimental Raman gain profile (blue circles) and its fit (red solid line) obtained with Eq. (3), and panel (b) displays overall fitted spectrum (dotted line) and twelve Gaussian components (solid lines of different colours).

A degree of compliance between the experimental Raman gain profiles and their counterparts calculated analytically can be seen from Fig. 2 for the reference GeO_2 -doped fibre. The same data for the TiO_2 -doped silica fibre under test is depicted in Fig. 3.

2.3. Verification of Gaussian decomposition for silica fibres

It is generally accepted in practical spectroscopy that the decomposition procedure performed in the case of strong overlapping of more than two vibrational modes cannot yield unambiguous separation of individual spectral contours. As a consequence, one might have reckoned that the sets of a dozen of Gaussian modes presented above cannot be considered as corresponding univocally to some framework of real oscillators that form the stimulated Raman spectrum. However, almost perfect coincidence of the calculated Raman gain profiles with the experimental data points to a very high accuracy of our decomposition procedure.

To elucidate further these points, we have analyzed the accuracy of the Gaussian decomposition for our silica fibres in a more detail. The discrepancies of our analytical model from the experimental data for GeO_2 - and TiO_2 -doped silica fibres are shown on a larger scale respectively in Fig. 4 and Fig. 5. In particular, the upper panel of Fig. 4 demonstrates a perfect coverage of the experimental Raman gain profile for the TiO_2 -doped fibre by its analytical form given by Eq. (3). Here the eleven Gaussian modes are defined by the parameters gathered in Table 1. We have picked out three different fragments of the Raman gain profile, which are denoted as I, II and III, with the respective spectral regions $100\text{--}200\text{ cm}^{-1}$ ($3\text{--}6\text{ THz}$), $400\text{--}500\text{ cm}^{-1}$

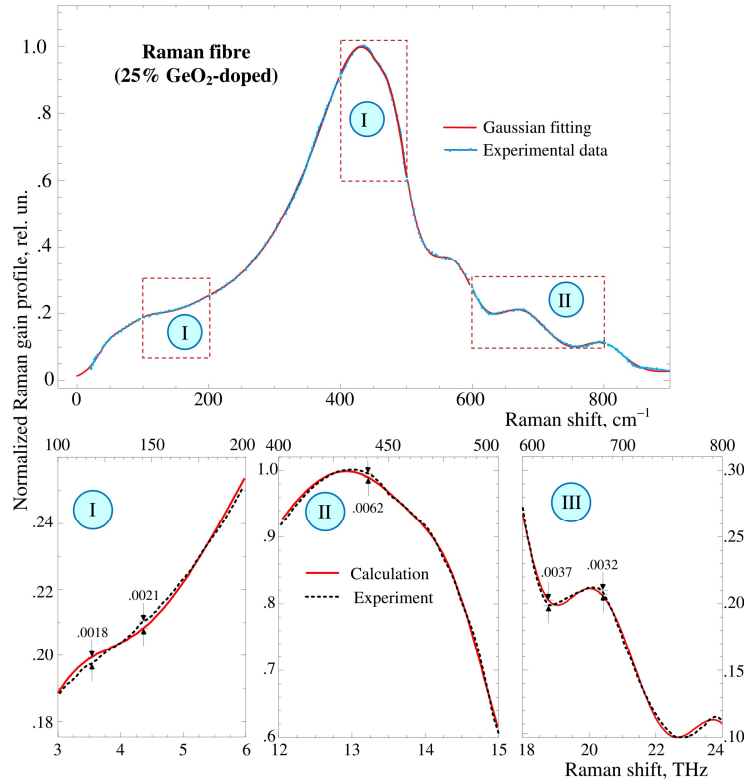


Fig. 4. Gaussian fit based on eleven modes, as obtained for the Raman-shifted region 0–900 cm^{-1} in GeO_2 -doped silica fibre (upper panel). Insets at the bottom illustrate fitting accuracies in the three parts of the gain profile: I – 100–200 cm^{-1} (3–6 THz); II – 400–500 cm^{-1} (12–15 THz), and III – 600–800 cm^{-1} (18–24 THz).

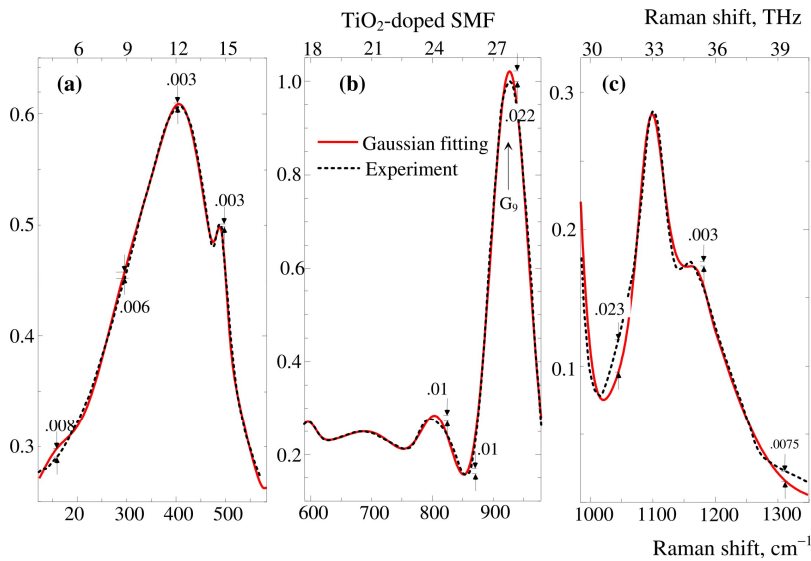


Fig. 5. Experimental Raman gain profiles for the TiO_2 -doped silica fibre (dotted lines) and their fitting with twelve Gaussians (solid lines). Different panels correspond to different spectral regions: (a) 200–600 cm^{-1} (6–18 THz), (b) 600–1000 cm^{-1} (18–30 THz), and (c) 1000–1300 cm^{-1} (30–39 THz).

(12–15 THz) and 600–800 cm^{-1} (18–24 THz). They are enlarged at the bottom panels of Fig. 4. As shown by arrows and the figures that describe the absolute theory–experiment discrepancies, the accuracy of the model remains not worse than 1% for any spectral point.

The results of modelling of the Raman gain profile for TiO₂-doped silica fibre are similar (see Fig. 5). Here we have marked out the following fragments: 200–600 cm⁻¹ (6–18 THz), 600–1000 cm⁻¹ (18–30 THz) and 1000–1300 cm⁻¹ (30–39 THz). Unlike the data for GeO₂-doped silica fibre, the spectrum of the TiO₂-doped fibre can deviate slightly stronger ($\geq 2\%$) from the model. Here the experimental Raman gain profile is fitted with the curve that involves twelve Gaussians. Although we have been unable to remove the 2% experiment–theory deviation observed for the Gaussian peak G₉ centred at 928 cm⁻¹ (see Fig. 5b), such a deviation value is less than the measurement accuracy. Of course, one could increase the fitting accuracy and remove the 2.3% deviation near the minimum at 1010 cm⁻¹ (see Fig. 5c) via adding more Gaussian modes. However, we consider this complication of the model as unjustified.

Summing up, the most interesting applied aspect of the Gaussian decomposition performed in our work consists in the fact that the analytical function $g_R(\omega)$ is capable of extremely accurate fit of the experimental Raman gain profiles. Of course, besides of the reasoning of maximal accuracy, the simplest sum in Eq. (3) with the least number of Gaussians is also preferable. Notice also that only the parameters A_i , $\omega_{v,i}$, and Γ_i with positive values have a strict physical meaning in the $g_R(\omega)$ formula (see Eq. (3)).

Therefore a computer procedure of nonlinear fitting has been used in our work and all the above argumentations have been taken into account. The best match has been obtained using a known Levenberg–Marquardt method, which represents a generalization of the common least-squares method for searching a minimum of objective function. In particular, very good fitting results have been obtained with a high-speed descent algorithm applied to the problem of quadratic minimization. As a result, the sums given by Eq. (3) for the both fibre types can be considered as practically exact analytical representations of the Raman gain profiles $g_R(\omega)$, since the appropriate calculation errors turn out to be essentially less than the random deviations in the experimental spectra.

Hence, one can directly determine the Raman gain profile while extracting the temperature-independent part from the spontaneous Raman scattering spectrum measured experimentally. Finally, an almost exact analytical form of the experimental Raman gain profile can result from a proper utilization of multi-mode decomposition. The above results provide a reliable basis for modelling of both FRLs and fibre Raman amplifiers.

3. Raman amplification threshold and absolute transparency of fibre

The physical meaning of Raman amplification threshold is achieving a state of complete optical transparency of a fibre due to compensation of fibre losses by nonlinear gain through stimulated Raman scattering. The threshold conditions may be derived directly from the well-known coupled-wave equations (see, e.g., Ref. [23]).

3.1. Absolute transparency function

Lossless propagation of a Stokes wave along the z -direction in a fibre implies that the Stokes intensity I_s remains constant along the z -coordinate. Then the expression $dI_s/dz = 0$ would define the condition for absolute transparency. Taking into account the condition $dI_s/dz = 0$ as a special point in the coupled-wave equations [23], one can derive the absolute transparency function

$P_p^{th}(\omega)$ in the following form:

$$P_p^{th}(\omega) = \frac{\alpha_s}{g_R(\omega)}, \quad (4)$$

with α_s denoting the absorption coefficient. The transparency function $P_p^{th}(\omega)$ given by Eq. (4) corresponds to the pumping power needed for achieving the lasing threshold as a function of Stokes-shifted frequency ω . Usually it is assumed that the approximation $\alpha_s \approx \alpha_p = \alpha$ (with α_s and α_p being the absorption coefficients respectively at the Stokes and pumping wavelengths) works well enough, whereas in practice the attenuations α 's do not change inside the whole band of Stokes-shifted components, $\sim 1000 \text{ cm}^{-1}$. Hence, after substituting the analytical form for the Raman gain profile $g_R(\omega)$ given by Eq. (3) into Eq. (4), one can also obtain analytical representation of the transparency function $P_p^{th}(\omega)$. Neglecting the loss variations over the transparency window near $1.55 \text{ }\mu\text{m}$, we have assumed that the absorption constant α_s is equal to 0.2 dB/km for the GeO_2 -doped fibre and 0.3 dB/km for the TiO_2 -doped fibre.

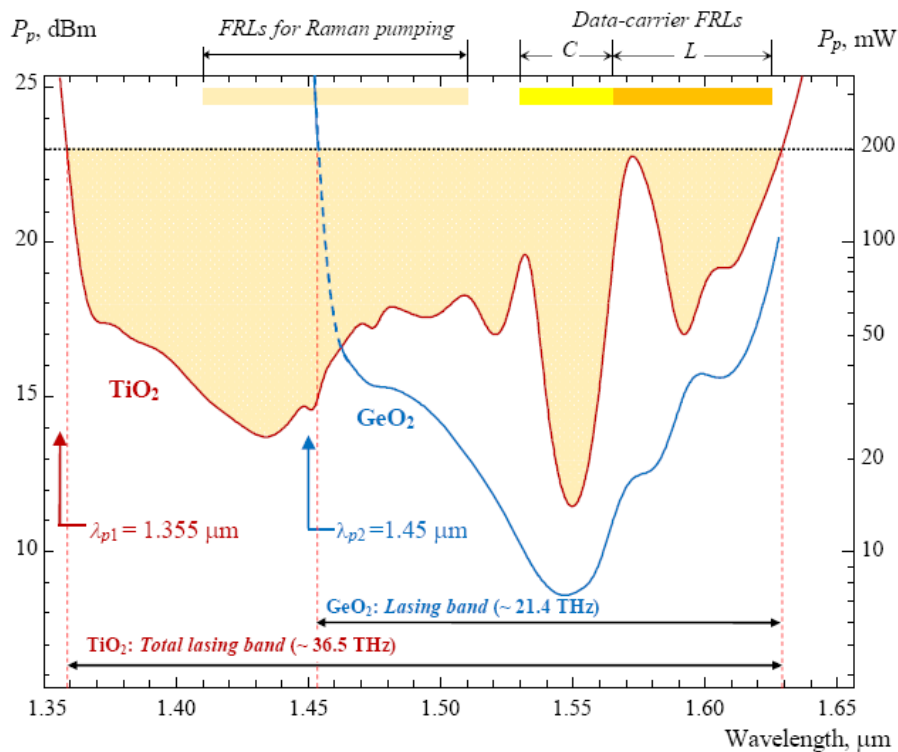


Fig. 6. Threshold Raman spectral profiles as functions of light wavelength for GeO_2 -doped (blue, $\lambda_p = 1.45 \text{ }\mu\text{m}$) and TiO_2 -doped (brown, $\lambda_p = 1.355 \text{ }\mu\text{m}$) silica SMFs. The whole lasing bands of GeO_2 and TiO_2 -doped fibres are compared at $P_p = 200 \text{ mW}$ (i.e., 23 dBm).

To illustrate the potentials of application of the absolute transparency function $P_p^{th}(\omega)$, we have compared the Raman gain bands in the GeO_2 - and TiO_2 -doped fibres at the pumping power 200 mW . Two pumping sources at $\lambda_p = 1.45 \text{ }\mu\text{m}$ (for the case of GeO_2 -based SMF) and $\lambda_p = 1.355 \text{ }\mu\text{m}$ (for the TiO_2 -based SMF) have been used in our simulations. The modelling results obtained for the Raman gain bands in the both SMFs are shown in Fig. 6. The above pumping parameters have been chosen to minimize the Raman threshold in the C-window ($\lambda = 1.55 \text{ }\mu\text{m}$) for

each of the SMF types. Simultaneously, TiO₂-based SMF can be used for a number of lasers and to carry signals at the wavelengths in the both C- and L-telecommunication windows.

3.2. Optical Raman amplification bandwidth and lasing band

Simulations of both the optical bandwidth and the lasing band for the Raman gain can be essentially simplified if one uses the transparency function $P_p^{th}(\omega)$ in its analytical form. In contrast to the GeO₂-doped SMF, the TiO₂-doped fibre has two main minima of the pump power (see Fig. 6). They correspond to the gain peaks located at 430 cm⁻¹ (13 THz) and 900 cm⁻¹ (27 THz) and associated with the Stokes-shifted frequencies.

The pumping parameters used to obtain the plots in Fig. 6 enable to reach a continuous optical Raman amplification in the TiO₂-doped SMF from 1.36 to 1.63 μm. Its total bandwidth amounts to ~36.5 THz when a single pump source is used. Such a Raman gain bandwidth is almost doubled if compared with the case of singly pumped GeO₂-doped SMF (21.4 THz). Moreover, this fibre can be used to produce low-power signal-carrying lasers and generate additional pumping sources for the fibre Raman amplifiers.

4. Conclusion

Summarizing, we have studied the Raman gain properties of the TiO₂-doped single-mode fibres, which can be applied in many photonic devices. The main Raman features of the TiO₂-doped SMFs have been compared with those peculiar for the most efficient (at the present time) active medium for the FRLs. This is the medium based upon highly GeO₂-doped Raman fibres. It is shown that, besides of a slight increase in the lasing threshold, a monochromatic working regime of TiO₂-based FRLs can be implemented. Then we obtain almost twice as wider spectral region, when compared with the lasing band typical for the GeO₂-doped fibre. These facts are confirmed by our modelling and numerical results. In particular, the continuous-lasing band for the TiO₂-doped single-mode fibres can be up to 270 nm at the relatively low pumping power (less than 200 mW). The Raman gain profile has been determined using the original spectroscopic method. It works on a reliable basis of fundamental theory and employs the experimental Raman cross-section of spontaneous scattering in the fibre under study. In the present work, we have used the standard spectroscopic procedure of multimode decomposition exclusively for the practical purpose of maximizing the accuracy of fit of the nonuniform Stokes continuum with the optimal number of Gaussian components. It has enabled us to obtain the analytical forms that provide very accurate fits of the experimental Raman gain profiles for the fibres under examination.

Acknowledgement

The authors acknowledge financial support of this study from the Ministry of Education and Science of Ukraine (the Project #0119U101296).

References

1. Dragic P D, Cavillon M and Ballato J, 2018. Materials for optical fiber lasers: a review. *Appl. Phys. Rev.* **5**: 041301.
2. Shi W, Fang Q, Zhu X, Norwood R A and Peyghambarian N, 2014. Fiber lasers and their applications. *Appl. Opt.* **53**: 6554–6568.
3. Syuaib I, Asvial M and Rahardjo E T, 2019. Modeling of ultra-long span bidirectional Raman transmission link using three-segment hybrid fiber core structure. *Photonics*. **6**: 18.

4. Pelouch W S, 2016. Raman amplification: an enabling technology for long-haul coherent transmission systems. *J. Lightwave Technol.* **34**: 6–19.
5. Downie J D, Hurley J, Roudas I, Pikula D and Garza-Alanis J A, 2014. Unrepeated 256 Gb/s PM-16QAM transmission over up to 304 km with simple system configurations. *Opt. Express.* **22**: 10256–10261.
6. Downie J D, Hurley J, Cartledge J, Ten S, Bickham S, Mishra S, Zhu X and Kobayakov A, 2010. 40×112 Gb/s transmission over an unrepeated 365 km effective area-managed span comprised of ultra-low loss optical fiber. In: *Proc. Eur. Conf. on Opt. Comm. (ECOC)*, Turin (Italy). 19–23 September, 2010.
7. Saidin N, Taib N I A, Abidin M S Z, Hasbullah N F and Ralib A A M, 2017. Performance configuration of Raman-EDFA hybrid optical amplifier for WDM applications. *IOP Conf. Ser.: Mater. Sci. Eng.* **210**: 012033.
8. Tan M, Rosa P, Le S T, Iqbal Md A, Phillips I D and Harper P, 2016. Transmission performance improvement using random DFB laser based Raman amplification and bidirectional second-order pumping. *Opt. Express.* **24**: 2215–2221.
9. Nelson L E, Zhou X, Zhu B, Yan M F, Wisk P W and Magill P D, 2014. All-Raman-amplified, 73 nm seamless band transmission of 9 Tb/s over 6000 km of fiber. *IEEE Photon. Techn. Lett.* **26**: 242–245.
10. Richardson D J, Nilsson J and Clarkson W A, 2010. High-power fiber lasers: current status and future perspectives. *J. Opt. Soc. Amer. B.* **27**: B63–B92.
11. Zervas M N and Codemard C A, 2014. High power fiber lasers: a review. *IEEE J. Sel. Top. Quantum. Electron.* **20**: 219–241.
12. Zhou P, Xiao H, Leng J, Xu J, Chen Z, Zhang H and Liu Z, 2017. High-power fiber lasers based on tandem pumping. *J. Opt. Soc. Amer. B.* **34**: A29–A36.
13. Ma P, Zhang H, Huang L, Wang X, Zhou P and Liu Z, 2015. Kilowatt-level near-diffraction limited and linear-polarized Ytterbium-Raman hybrid nonlinear amplifier based on polarization selection loss mechanism. *Opt. Express.* **23**: 26499–26508.
14. Xiao Q, Yan P, Li D, Sun J, Wang X, Huang Y and Gong M, 2016. Bidirectional pumped high power Raman fiber laser. *Opt. Express.* **24**: 6758–6768.
15. Feng Y, Taylor L R and Calia D B, 2009. 150 W highly-efficient Raman fiber laser. *Opt. Express.* **17**: 23678–23683.
16. Dianov E M and Prokhorov A M, 2000. Medium-power CW Raman fiber lasers. *IEEE J. Sel. Top. Quant. Electron.* **6**: 1022–1028.
17. Dianov E M, 2002. Advances in Raman fibers. *J. Lightwave Technol.* **20**: 1457–1462.
18. Felinskyi G S, Serdeha I V and Grygoruk V I, 2017. TiO₂-doped singlemode fiber as active medium for Raman lasers. *Key Eng. Mater.* **753**: 173–179.
19. Bromage J, Rottwitt K and Lines M E, 2002. A method to predict the Raman gain spectra of germanosilicate fibers with arbitrary index profiles. *IEEE Photon. Technol. Lett.* **14**: 24–26.
20. Mermelstein M D, Horn C, Radic S and Headley C, 2002. Six wavelengths Raman fiber laser for C- and L-band Raman amplification and dynamic gain flattening. *Electron. Lett.* **38**: 636–638.
21. Korotkov P A and Felinskyi G S, 2009. Forced-Raman-scattering-based amplification of light in onemode quartz fibers. *Ukr. J. Phys. Rev.* **5**: 103–168.
22. Zhang L, Liu C, Jiang H, Qi Y, He B, Zhou J, Gu X and Feng Y, 2014. Kilowatt ytterbium Raman fiber laser. *Opt. Express.* **22**: 18483–18489.

23. Serdeha I V, Grygoruk V I and Felinskyi G S, 2018. Spectroscopic features of Raman gain profiles in single-mode fibers based on silica glass. Ukr. J. Phys. **63**: 683–700.

Felinskyi G. S., Grygoruk V. I. and Serdeha I. V. 2020. Modelling of gain profiles and Raman lasing in TiO₂/GeO₂-doped silica fibres. Ukr.J.Phys.Opt. **21**: 15 – 25.

doi: 10.3116/16091833/21/1/15/2020

***Анотація.** На основі моделювання профілю підсилення проаналізовано ширину смуги пропускання раманівського лазера для легованого TiO₂ одномодового волокна як функцію потужності нагнітання. Виконано порівняння з типовими параметрами еталонного раманівського волокна, легованого GeO₂. Обидва профілі раманівського підсилення оцінено кількісно на основі спонтанних раманівських перетинів, одержаних за оригінальним спектроскопічним методом. Для профілів раманівського підсилення одержано надзвичайно високу точність розкладання спектрів на гаусових мод. Як наслідок, профілі раманівського підсилення можна представити в аналітичній формі. Введено пороговий спектральний раманівський профіль і чисельно промодельовано лазерні смуги для обох одномодових волокон. Обговорено переваги волокон, легованих TiO₂, як активних середовищ для раманівського волоконних лазерів, а також порівняно їхні характеристики з характеристиками інших типів волокон.*